Journal of Design Against Fatigue, Vol. 3, No.1 (2025) 37-49

Journal of Design Against Fatigue
https://minerva-aset.com/JDAF
MINERVA ASET
ISSN 2976-940X

Fracture Analysis of Copper Cathode and Function Optimization of the Cathode Stripping Machine (CSM)

Mohsen Forouzanmehr[1], Mohammad Reza Dashtbayazi[1,*], Masoud Raoufi Jahromi[1], Seyedhamed Pourbagheri[2]

[1]*Department of Mechanical Engineering, Faculty of Engineering, Shahid Bahonar University of Kerman, Kerman, Iran.*

[2] *Engineering and Technical Division, Research and Development Department, Sarcheshmeh Copper Complex, Rafsanjan, Iran.*

P A P E R I N F

Paper history:
Received 04 May 2025
Received in revised form 30 May 2025
Accepted 02 June 2025

Keywords:
Cathodes Stripping machine, Cathode, Cathode Blank, Pure Copper Cathode, Fracture Mechanics, FEM, CZM.

A B S T R A C T

Incorrect separation of the copper cathode from the stainless-steel cathode blank in the cathode separation machine (CSM) is a significant factor affecting production efficiency. This study investigates the conditions leading to improper cathode separation and explores ways to address this issue. Experimental observations show that the thickness of the cathode, the formation of nodules on the cathode, and the positioning of the flex mechanism in the (CSM) significantly influence the separation of cathodes from the cathode blanks. Once, twenty-four cathodes were randomly selected from the CSM output at Sarcheshmeh Copper Refinery (Rafsanjan, Iran). The thickness, crack width and length in the cathodes separated from the cathode blanks were measured. Subsequently, after model validation and simulation strategies, the cathode separation process, involving the application of impact by the flex, was simulated using the finite element method (FEM) with the cohesive zone model (CZM). In the FEM simulation, CZM was applied under the assumption of plane strain and considering fracture energy to predict the changes in the separation layers of the cathode from the cathode blank. Simulation results indicate that shifting the position of the flex increases the crack width and length of the cathode-cathode blanks separation. Finally, based on the simulation results, a mechanism to optimize the impact location for more efficient cathode separation was designed, and improved the machine for CSM in practice.

https://doi.org/10.62676/jdaf.2025.3.1.30

1. INTRODUCTION

The final stage of the pure copper sheet production cycle, in the electrorefining process, involves the separation of copper cathode from the stainless-steel cathode blank, as in concisely, cathode and cathode blank, respectively [1]. During the electrorefining process, the cathode is deposited as two layers of copper metal onto the cathode blank through the electrolysis process. The real output of the electrorefining process forms a material as a sandwich-like composite. Issues that arise after the electrorefining process in the production of the pure copper sheet include: the detachment of rubber edges, which causes copper welding on both sides of the cathode, copper cathode-blank separation, and the formation of nodules on the coated copper cathodes. In advanced cathode stripping machines (CSMs), initial separation of cathode is performed by two mechanical impact members [2]. During the cathode separation process in the CSM, issues such as non-optimal impact, which causes insufficient energy separation layers, and the spring back of the cathode blank [3], resulted in incomplete separation of the cathode from the cathode blank. An optimal impact generates the maximum separation or fracture energy between the cathode and the cathode blank [4].

In the copper production industry, various machines are utilized for cathode separation. The ISA 2000® CSM system [2] uses hydraulic knives to separate the cathode from the cathode blank, opening the copper sheet to a 60-degree angle before flattening it using clamps and impactor mechanisms [2]. If complete separation is not achived, the turnover mechanism repeatedly moves until fracture and detachment of the copper sheet occurs.[1]. The ISA 2000 and KID CSM Flex Stripper feature hydraulic knives that span the entire width of the copper sheet, applying force uniformly across the cathode blank and the copper cathode. This system is particularly effective in separating the cathode from the cathode blank, especially in the corners [5]. A second knife is employed for more challenging separations. However, despite its suitability for space and cost constraints, the separation process in this system is relatively time-consuming. The CSM ISA Roller Stripper® utilizes conical rollers, designed to match the length of the cathode, to apply separation forces while also serving as supports. The upper roller holds the cathode in place and supplies the necessary separation force. The middle roller provides both

*Corresponding Author Email: *dashtbayazi@uk.ac.ir*

support and additional separation force. A second roller applies horizontal force, while the final roller serves as a backup support in case the separation is incomplete, repeating the cycle if necessary [1].

In the context of damage in sandwich composite materials, which is a key concern in the failure of cathode separation from the cathode blank, several studies have explored this topic. Volpi et al. [6] investigated damage prediction in sandwich composite panels under low-velocity impact using the finite element method (FEM) to simulate the structural response and vulnerability of foam-based sandwich composites subjected to low-speed impacts. The initiation and propagation of damage were analyzed, and FEM results were compared with experimental impact test data from carbon/epoxy sandwich panels. A satisfactory correlation was found between simulations and experiments, confirming the model's capability to predict impact damage characteristics, damage extent, and delamination at various depths. Similarly, Höwer et al. [7] conducted finite element modeling of cohesive zone separation for mode I delamination between the face sheets and core of sandwich panels. Their results were validated through force-displacement experimental data, demonstrating strong agreement. A specialized formulation was developed to model fracture, adhesion, and bridging mechanisms governing the separation process. Their methodology was applied to honeycomb aluminum sandwich structures, with results showing a high correlation with experimental data. Face sheet/core debonding in aluminum foam sandwich panels (AFSP) during plastic forming was numerically analyzed using a bilinear cohesive zone model (CZM) [8]. Experiments and simulations characterized CZM parameters and extensive simulations on spherical and saddle-shaped AFSPs provided insights into debonding behavior. Results showed that reducing adhesive initial stiffness and increasing maximum traction and critical fracture energy can prevent debonding failure.

Correia et al. [9] analyzed the performance of curved bonded joints (SLJ) using carbon fiber-reinforced polymer (CFRP) adherents, considering three adhesives (brittle, moderately ductile, and ductile). Using the Finite Element Method (FEM) and Cohesive Zone Model (CZM), the effects of geometric parameters such as overlap length, adherent thickness, and curvature radius on joint strength and energy dissipation were analyzed. Results showed that increasing overlap length improved performance for ductile adhesives, while larger adherent thickness reduced strength. The brittle adhesive was less sensitive to these changes. This study provides effective design guidelines for optimizing curved joints in aeronautical applications.

Furthermore, Aryal et al. [10] examined the effects of impact energy, velocity, and impactor mass on damage evolution in the composite layers of sandwich panels. Their FEM model was validated with experimental data, revealing that multi-layered structures exhibited higher strength than single-layer composites. Moreover, the shape of the impactor significantly influenced damage propagation: sandwich panels demonstrated the highest resistance to flat impactors and the lowest resistance to conical ones. The kinetic energy of the impactor was found to be distributed into four components: internal energy of the core, internal energy of the face sheets, and frictional energy, all of which played a significant role in energy absorption.

In the subject of stripping, Almeida et al. [11] investigated the zinc deposit stripping behavior using FEA and experiments, focusing on deposit thickness, adhesion strength, cathode roughness, and repeated plating cycles. Results showed increased roughness and adhesion with repeated use, while FEA highlighted bending force as the primary stripping component. The findings offer insights for optimizing plating processes to reduce zinc sticking, improve productivity, and lower costs.

Chen et al. [12] investigated the copper/Q235 steel/copper composite block with strong bonding interfaces that was successfully fabricated using explosive welding, a promising technique for laminate production. The interfaces were analyzed using tensile-shear tests, OM, XRD, SEM, and EBSD, revealing shear strengths exceeding ~235 MPa (upper interface) and ~222 MPa (lower interface). Failure occurred within the copper layer, not at the interface, due to the absence of defects and the formation of metallurgical bonding with ultra-fine grains, enhancing plastic deformation coordination and inhibiting micro-crack formation.

From an engineering design perspective, the aforementioned studies have focused on modeling and experimental testing to develop optimized structures and methods for minimizing damage in laminated composite materials. However, in manufacturing industries, controlled damage rather than damage prevention is sometimes the primary objective. This research aims to induce controlled damage (i.e., layer separation of copper-stainless-steel sandwich composites, resulting in crack initiation and propagation) to enhance the separation of composite layers, consisting of the copper cathode and the stainless-steel cathode blank, in the copper cathode process used in copper production industries. In this study, the industrial system used for cathode separation in the Sarcheshmeh Copper Refinery Complex is described. This paper investigated the thickness of formed cathodes and its statistical relationship with length and width of formed cracks in the laboratory section. The statistical results showed that the thickness of the deposited copper can significantly influence the dimensions of induced cracks and impact-induced delamination. Subsequently, considering the mean values and studied statistical population, finite element analysis of delamination was performed, using cohesive zone modeling (CZM). Finally, an optimized mechanism to adjust the impact location in the CSM is proposed for improved efficient.

2. CSM OPERATION DESCRIPTION

The Sarcheshmeh Copper Complex in Rafsanjan is one of Iran's largest copper processing and refining facilities [13]. Fig. 1 provides an overview of the copper refining process. Its production process in the refinery includes multiple stages: anode storage and classification, electrolytic refining, cathode stripping, and anode scrap collection. In the electrorefining hall, copper is deposited on the stainless-steel cathode blank, forming a copper cathode. These cathodes undergo pressing, washing, and classification before separation. The cathode stripping line plays a key role in separating the copper sheet from the stainless-steel cathode blank using mechanical stripping in CSM. Ensuring efficient cathode separation is critical to maintaining productivity and quality, making this stage a key focus for process optimization. The electrorefining process involves placing copper anodes produced from smelting and typically 99.5% pure alongside 316 stainless-steel cathode blanks in sulfuric acid (H_2SO_4) electrolyte baths [14]. A controlled voltage is then applied to facilitate the deposition of 99.997% pure copper onto the stainless-steel cathode blanks. During the process, the impure copper anodes dissolve into the electrolyte as Cu^{2+} ions, while pure copper is electrodeposited onto the stainless-steel cathode blanks [15]. Upon completion, the final product consists of stainless-steel sheets sandwiched between two layers of pure copper, resembling a sandwich composite structure. These copper-coated cathode assemblies are then transferred via overhead cranes to the cathode stripping line, where specialized mechanical separation devices detach the copper layers from the stainless-steel substrates. The cathode stripping unit (made by BROCHOT Co., French) consists of three main sections: the cathode separation station, the discharge section for the separated pure copper sheets, and the exit station for the stainless-steel cathode blanks, which are reintroduced into the electrorefining cells.

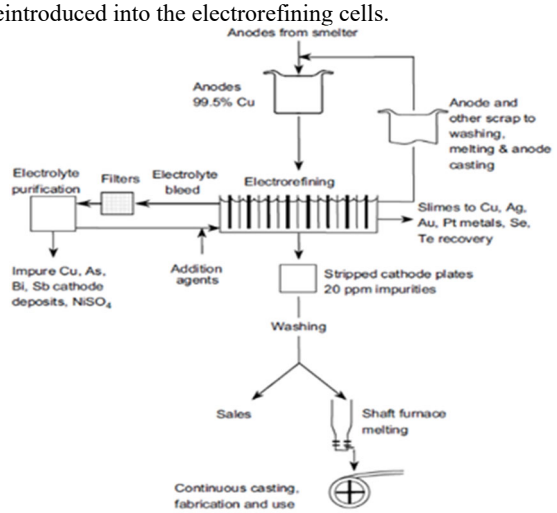


Figure 1. Electrolytic refining process in the Copper refinery [1]

Fig. 2 presents a schematic of the CSM. The handling and sorting of the cathodes and emptying the cathode blanks are performed by three robotic systems. In the first step, before the separation station, cathodes and cathode blanks are weighed at the weighing station, an operation performed by Robots 1 and 2. Due to the low significance of the weighing station, Robots 1 and 2 (KUKA Co., Germany) are not illustrated in Fig. 2.The replacement of copper-steel-copper for separation of the pure cathodes is then executed by Robot 3. This robot is responsible for positioning and separating the cathodes using mechanical separators at the stripping station. Fig. 2a illustrates Robot 3, including its gripping arm. Fig. 2b shows the stripping mechanism, including the cutting system and impactor used for cathode separation. A zoomed-in view of the cutting and impact mechanism, also referred to as the "flex" is depicted in Fig. 2c. At this stage, the composite cathode assembly (copper-steel-copper) undergoes controlled impact at a constant low velocity (0.002 mm/s), applied laterally to the composite sheet. Subsequently, the vertical movement of the cutting blades, shaped in a wedge-like configuration, facilitates the fully separation of the cathode from the cathode blank (Fig. 2c). Finally, the U-shaped cathode is discharged at the end of the stripping process and transported to the final processing line, where they are pressed, packaged, and prepared for shipment outside the refinery.

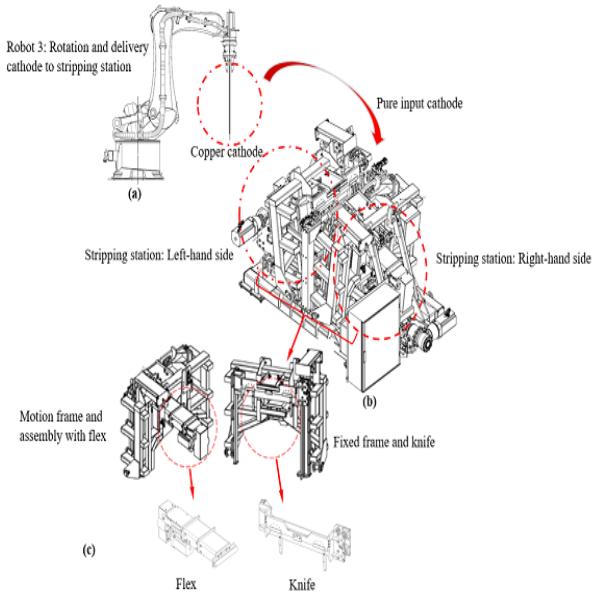


Figure 2. Overview of the Sarcheshmeh CSM, a) the robot delivering the composite cathode to the stripping section, b) the stripping section, c) zoom-in view of the important strip ping details, including knife cutters and impact flex

As shown in Fig. 3, in the first stage (Fig. 3a), constraints acting as holders are applied from both sides to prevent movement of the generated composite consisting of the cathode and the cathode blank. These constraints exert constant pressure on the sides of the sandwich composite sheets at the lower section of the machine (One-fifth from the lower end of the device). Then, the right-side flex strikes the cathode at an approximate distance of 300 millimeters from the upper edge of the sheets. If successful, this impact separates the upper edge of the cathode on the right side from the cathode blank (Fig. 3b). Subsequently, the left-side impactor delivers a similar impact, leading to the separation of the upper edge of the cathode on the left side of the cathode blank. Finally, the cathode is completely

separated from the cathode blank by cutting blades, and after the release of the support constraints in (Fig. 3c), it exits from the lower section of the machine (Fig. 3d).

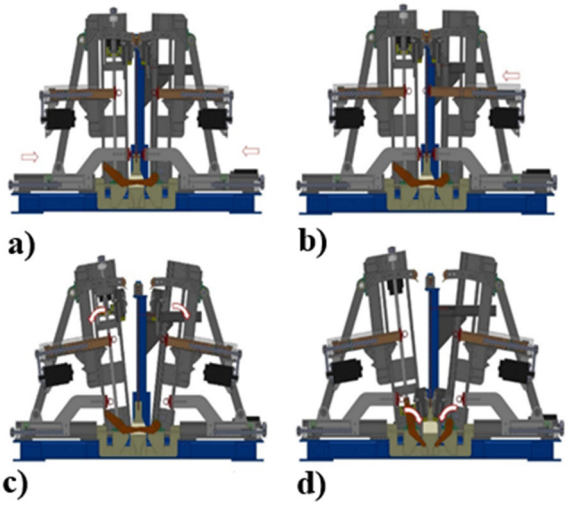


Figure 3. Schematic of the cathode separation process in CSM. (a) application of holding constraints, (b) impact applied by the right-side striker (as indicated), (c) separation of the cathode from the cathode blank in the upper region of the cathode sandwich panel, (d) complete separation and discharge of the cathode from the blanks

3. MATERIALS AND METHODS

Due to the frequent stoppages of the CSM and the failure of the cathode separation under the impact of the flex [2], an optimized analysis of the impact position and its effect on separation is necessary. In this section, the separation process is thoroughly examined, considering the operational mechanism of the CSM. Given the continuous operation of this machine in the refinery and the constraints on halting the process, data collection was performed only during machine failure in the separation process. Initially, a detailed audit of the separation process was conducted, taking into account the experimental setup (including the CSM and the behavior of the formed sandwich composite structure). By framing the separation problem within the context of fracture mechanics, the fracture behavior of the CSM was analyzed. Experimental and numerical methods and mechanism design were employed to propose an optimized solution for the separation issue. All analyses, expected cohesive parameters of Rafsanjan refinery elctrorefining tank house processes, were based on the mechanical behavior of stainless steel (SS 316) and commercially pure copper as documented in the literature [16, 17].

4. INSPECTION AND AUDIT OF THE CATHOD STRIPPING SYSTEM

To assess the audit and extent of the cathode separation from the cathode blank due to impact in CSM, a sampling process was conducted over 14 days. Given the operational limitations, including machine stoppage and potential disruptions to production, samples were collected randomly during both day and night shifts. A total of 24 samples were selected from the CSM's output, consisting of a sandwich composite structure with a core of stainless steel (SS 316) layer in the center and two layers of the copper cathode on either side. Before separation, the average thickness of the copper deposited on cathode blanks was measured across the length and width of the cathode using a micrometer. After the impact was applied by the stripping machine's flex, the right side of the machine was halted in coordination with the operator to allow for measurement. The width of the opening (crack) at one side of the cathode separating from the cathode blank was recorded at four points along the opening length. As shown in Figure 4, the measurements were taken at points A, B, C, and D, spaced at one-quarter intervals along the total crack length from point A to point E. In summary, the transverse openings were quantified using four parameters (A, B, C, D), corresponding to positions at one-quarter, two-quarters, three-quarters, and the full length of the opening (point of E).

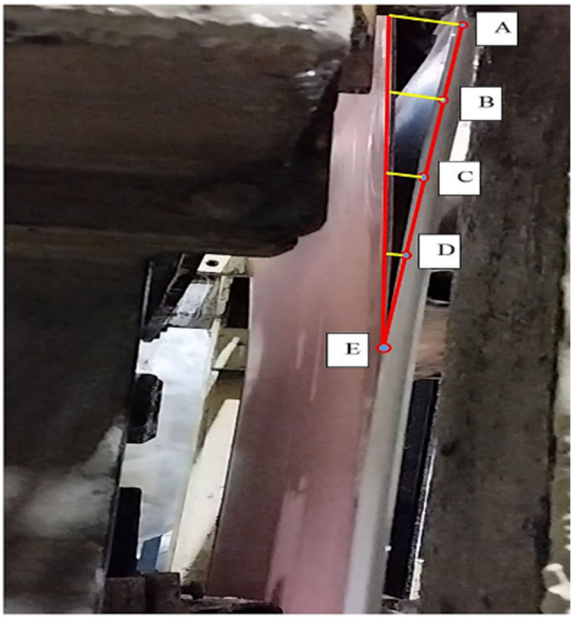


Figure 4. The copper cathode separated from the stainless-steel cathode blank after impact applied by the flex in the CSM

5. NUMERICAL ANALYSIS

Concerning the nature of the cathode separation from the cathode blank, the finite element model based on the cohesive zone method has been used. In this method, the cohesive zone is modeled either as a surface or as an element. When the likelihood of separation and crack propagation in materials with a delamination type occurs, the numerical damage solution using the traction-separation law and cohesive zone elements is effective [18]. This method relies on the assumption of element removal by considering the reduction or degradation in the material's stiffness as the progression of damage, separation, or

delamination between the cohesive surfaces. Initially, we will investigate the theories applied by validating the existing results in the literature in solving the separation problem. Cohesive zone elements in Abaqus 2022, solve two types of problems: 1- Adhesive connections include: a cohesive layer with finite thickness, for materials with known properties [18], 2- Delamination problems include: a cohesive zone with zero thickness, especially for bulk materials with unknown properties of the cohesive region [19]. To this end, we will investigate the relationships used in solving the problem. Considering the two composite plates of copper and stainless steel (SS 316), and assuming the materials are isotropic, their elastic behavior is described with Young's modulus and Poisson's ratio (E, ϑ). The constitutive relationships are expressed through the stress-strain relation in the cohesive zone [20] by Eq. 1 . In this relation, the nominal stress refers to the force components divided by the initial cross-sectional area, and the nominal strain refers to the displacement components divided by the thickness of the cohesive zone at the accumulated finite element nodes. The nominal strain refers to the displacement components divided by the thickness of the cohesive zone at the accumulated finite element nodes. This thickness varies in different problems. For the first method, the stress-strain relationships are:

$$\mathbf{t} = \begin{Bmatrix} t_n \\ t_s \\ t_t \end{Bmatrix} = \begin{bmatrix} K_{nn} & K_{ns} & K_{nt} \\ K_{ns} & K_{ss} & K_{st} \\ K_{nt} & K_{st} & K_{tt} \end{bmatrix} \begin{Bmatrix} \varepsilon_n \\ \varepsilon_s \\ \varepsilon_t \end{Bmatrix} \quad (1)$$

Where t is the nominal stress vector, including three components: t_n and t_s for the 2D stress components, while t_t corresponds to the 3D simplified case. The components $K_{i,j}$ refers to the elastic stiffness matrix of the cohesive zone material. ε_n, ε_s, ε_t, are the nominal strain components. In Eq. (1), the nominal stress is the force components divided by the initial cross-sectional area, and the nominal strain is the displacement components divided by the cohesive zone thickness that varies in different problems at the integration points of the finite elements. The strain components are expressed as:

$$\varepsilon_n = \frac{\delta_n}{T_0}, \varepsilon_s = \frac{\delta_s}{T_0}, \varepsilon_s = \frac{\delta_t}{T_0} \quad (2)$$

In which, δ_n ,δ_s and δ_t represent the displacement components at the initiation of separation. T_0 is the thickness of the cohesive zone element. In Abaqus 2022, Young's modulus is considered the final elastic stiffness of the material for the traction-separation law. For instance, considering the opening mode, the following relationship can be applied, based on the force-displacement curve [21]:

$$K_{nn} = \frac{N_{max}}{\delta_n^{init}} \quad (3)$$

In Eq. (3), as shown in Fig. 5, N_{max}, represents the maximum applied force, and δ_n^{init} is the displacement at the initiation of damage, based on the fracture modes (opening, shear loading, or combined). In Abaqus, nominal stress and strain values are considered, and based on this, the elastic response of the material will be computed using K_{nn}. If a non-unit thickness (1) is used for the cohesive zone elements, the information should be appropriately included in the material stiffness matrix as per the element thickness. Fig. 5 shows the behavior of two materials, linear and nonlinear, with energy levels. In this graph, G_{TC} represents the fracture energy, and δ_n^{fall} indicates the complete failure and full separation of the cohesive zone. To calculate K_{nn}, the following equations are used in Abaqus 2022:

$$N = E_n \varepsilon_n = K_{nn} \delta_n \quad (4)$$

$$\varepsilon_n = \delta_n / h_{eff}$$

In Eq. 4, h_{eff} represents the thickness of the cohesive zone. By combining Eq. 3 an, the following relationship is obtained as:

$$K_{nn} = \frac{E_n}{h_{eff}} \rightarrow E_n = K_{nn} h_{eff} \quad (5)$$

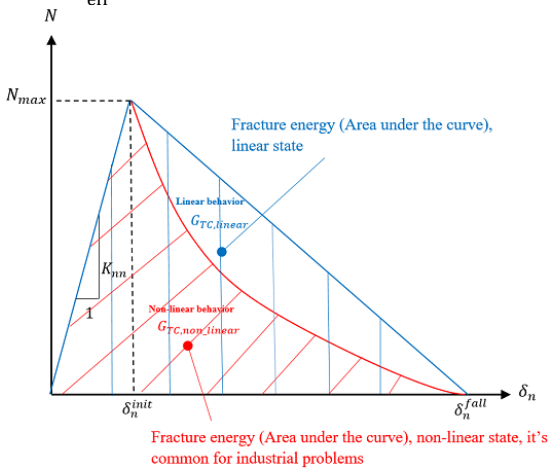


Figure 5. Force-displacement diagram of the cohesive zone and fracture energy levels for materials with linear and nonlinear behavior

This value, after calculating the fracture energy under shear conditions, results in the following parameters considering the failure loading mode (normal or shear). The traction-separation law involves three parameters: $E_{nn} = \frac{E}{K_{nn}}$ ،$G_{ss} = \frac{G1}{K_{ss}}$ and $G_{tt} = \frac{G2}{K_{tt}}$ which correspond to the nominal stress in the primary loading direction and the nominal shear stresses, respectively. The damage behavior in adhesive layers can be modeled using three damage mechanisms: initial failure criterion, damage evolution, and element deletion at complete failure. The quadratic damage initiation criterion is used to predict damage in cohesive zone elements between layers, incorporating the traction-separation behavior. This principle evaluates the stress ratio between the given stress value and the maximum nominal stress value. Accordingly, damage initiation occurs when the squared sum of the nominal normal and shear stress ratios equals one [22]:

$$\left(\frac{\langle \sigma_n \rangle}{N_{max}}\right)^2 + \left(\frac{\sigma_s}{S_{max}}\right)^2 + \left(\frac{\sigma_t}{T_{max}}\right)^2 = 1 \quad (6)$$

where, σ_n ،σ_s and σ_t represent the nominal normal stress, the first shear stress, and the second shear stress in the loading plane, respectively. To define the energy at the failure point, damage accumulation is considered based on either energy or displacement. As shown in Fig. 5, the area under the force-displacement or stress-displacement curve for the cohesive zone element up to the failure point (G_{TC}) is used as a criterion

for assessing damage accumulation in cohesive zone elements. Assuming homogeneous conditions in the bonding region, the energy release modes (Mode I, Mode II, and Mode III) reduce to Eq. 7:

$$G_{IC} + G_{IIC} + G_{IIIC} = G_{TC} \quad (7)$$

In the second approach, the cohesive zone is modeled using surface-based cohesive behavior, where the cohesive interaction is defined at the contact surfaces rather than using explicit cohesive elements. This method assumes a cohesive layer with nearly zero thickness, and the adhesive mass is neglected. The damage parameters are then defined at the contact interface. In the following, the validation of the modeling process is discussed.

6. VALIDATION AND NUMERICAL SOLUTION

To investigate and validate the issue of the separation of copper cathode, reference data [23] was utilized. For the optimization and analysis of the results, in the first phase, an aluminum-aluminum bonded joint using graphene-epoxy nano-adhesive was considered, based on the experimental data from the aforementioned study. The specifications of this joint included a length of 85 mm and an adhesive thickness of 0.2 mm. Fig. 6 illustrates the molded sample with the punch and die, as well as the adhesive region.

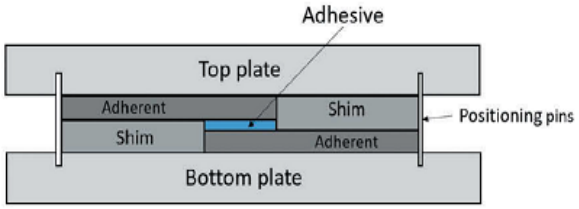


Figure 6. Schematic model for simulation validation

The elastic properties of the isotropic aluminum material, including Young's modulus and Poisson's ratio, were defined as E = 70 GPa and ν = 0.35, respectively. To characterize the adhesive region, nominal stresses (both normal and shear) and fracture energy were calculated. In Abaqus software, the stress-strain relationship was transformed into a stress-displacement curve. This issue was addressed by multiplying the thickness of the adhesive region by the strain. The resulting properties are summarized in Table 1. Considering the solution of the two-dimensional plane strain problem, the nominal elastic parameters of the material related to the traction-separation law were assumed to be identical in shear mode. Additionally, all damage components in Eq. (4) were defined with a value of 27 MPa.

TABLE 1. Mechanical properties of the adhesive region

$\frac{E}{K_{nn}} = 7980\ \mathrm{N/mm}$
$\frac{G1}{K_{SS}} = \frac{G2}{K_{tt}} = 2852\ \mathrm{N/mm}$
Damage initiation parameter = 27 MPa
$G_{TC} = 0.08 \times 27 = 2.01\ \mathrm{N/mm}$

After introducing the properties inferred from experimental results into the software, the boundary conditions were applied as follows: a displacement load (1 mm) was applied at one end of the joint on the top-right corner node of the geometry, while complete motion constraints (fixed boundary condition) were applied at the other end (on the line), as shown in the Fig. 7. In the generated file, the adhesive layer is depicted at the center of the joint.

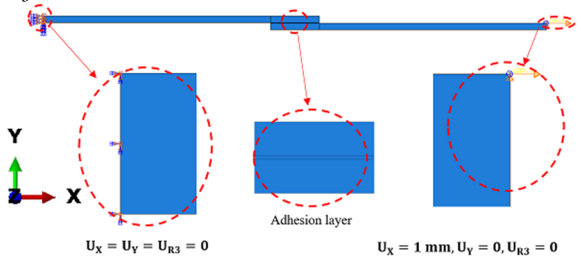


Figure 7. The model was created in the software, and boundary conditions

Fig. 8 illustrates the meshing of the finite element model. As shown in Fig. 8, CPE4R elements were used for the aluminum joints, while COH2D4 elements were employed for the adhesive region. The maximum damage ratio for the adhesive region elements, according to Eq. 4, was set to one, and the linear bulk viscosity was assumed to be 0.1.

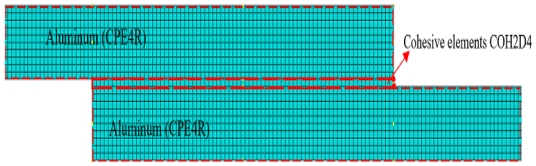


Figure 8. Meshing of the finite element model along with the elements used in it.

After applying the loading, the maximum force exerted on the joint was compared with the experimental results. As shown in Fig. 9, the contour of the reaction force corresponds to the maximum force applied to the joint. In this figure, the variation in magnitude (contour) and direction of the reaction force at the support (i.e., the primary force acting on the joint assembly) is shown to be constant. According to the figure, the applied force obtained from the numerical results is $\mathrm{RF_{FEM}} = 5014$ N, which, compared to the experimental results of $RF_{EXP.} = 5100\ N$, exhibits an error of approximately 2%.

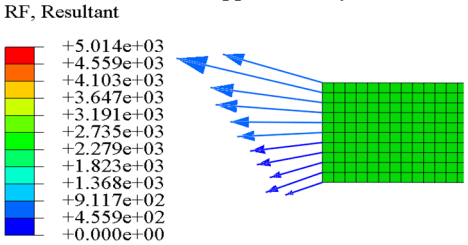


Figure 9. Maximum force obtained at the loaded node

Subsequently, to investigate the separation, the stress contours of the elements at maximum loading, during separation, and at complete separation (failure) are shown in Fig. 10. As illustrated in the figures, the applied stress decreases significantly with crack propagation (element deletion) in Fig. 10b and 10c, and it approaches nearly zero at complete separation (Fig. 10d).

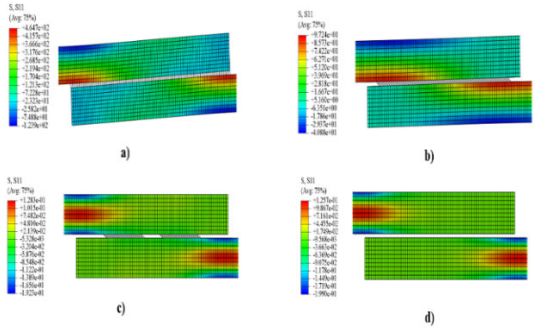


Figure 10. (a) Maximum stress applied to the joint elements, (b) progression of separation (element deletion), (c) damage at the threshold of separation, (d) complete separation.

7. FINITE ELEMENT MODELING

Following a comprehensive validation of the theoretical framework and methodologies for addressing separation phenomena in Abaqus 2022, this study proceeds to model the separation of the copper cathode from the stainless-steel cathode blank. Given the absence of precise data regarding the interfacial thickness formed between the copper and the stainless steel, a surface element approach incorporating contact interactions is adopted. The separation process is simulated under quasi-static displacement conditions, reflecting the low-velocity (v = 0.003 mm/s) flex impact applied to the cathode sandwich composite structure. The mechanical properties of the copper and stainless steel are addressed in Table 2.

Table 2. Mechanical properties of copper and stainless steel.

Material	Density (ton/mm³)	Young's Modulus (MPa)	Poisson's Ratio
Copper	0.00896	117	0.34
Steel	0.00798	200	0.28

The geometry of the sandwich composite structure, formed during the electrorefining process at the Sarcheshmeh Copper Complex, was meticulously dimensioned. The position of the flex, part names, and the cathode formed on the cathode blank were accurately modeled, as illustrated in Fig. 11. The figure also specifies the dimensions of the impact hammer (500 mm in length) and the side holders of the composite assembly, which measure 780 mm in length. The stainless-steel blank dimensions were defined as 1100 × 960 × 3 mm³, while each layer of the formed pure copper sheet was modeled with dimensions of 1000 × 960 × 7 mm³. The longitudinal distance of the flex in the cathode stripping section, under non-optimal conditions, was defined as 330 mm from the edge of the formed copper to the impact line (Figs. 11 and 12). By maintaining a constant transverse displacement of the flex at the impact line and varying its position, the study aimed to identify the configuration that maximizes the force applied to the structure, as determined by the numerical results. This configuration was designated as the optimal separation point. By systematically varying the position of the flex while keeping its transverse displacement constant, the study identified the optimal separation location based on the loading in the numerical results.

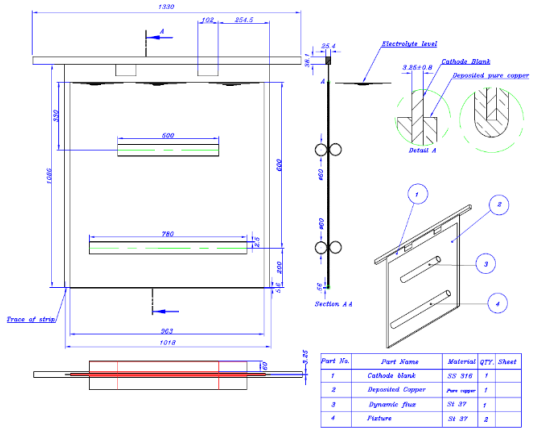


Figure 11. Geometry depicted based on the position of the punch flex and the copper loading dimensions on the cathode blank

The properties of the adhesive interface formed between copper and steel during the electrorefining process do not have a specific, precise value. Residual stresses were excluded from the modeling based on the assumption of stress-relieved cathode blanks (periodically treated in the plant to prevent spring back). Since the study focused on defect-free cathodes (deflected and aging cathodes), residual stresses were negligible in the analyzed scenario. The defined values in this section, due to the lack of real experimental data on adhesion strength and fracture energy of the adhesive zone, are estimated based on the analysis of the opening displacement and separation under the displacement of the flex position through a trial-and-error approach. The results approximate the damage properties and fracture energy (Eqs. 4 and 5) in the contact region, as mentioned in Table 3.

Table 3. Properties of the adhesion zone

Parameter	Symbol	Value	Unit
Normal stress	σ_n	50	KPa
Shear stress (1)	σ_s	30	KPa
Shear stress (2)	σ_t	30	KPa
Fracture energy	G_{TC}	0.2	N/mm

To apply boundary conditions, two holding constraints are placed at both ends of the copper cathode sheet, and a fixed boundary condition is applied to the top of the steel sheet, restricting movement in the three main directions and torque. It is worth noting that during loading, the punch applies a force at a distance of 330 mm from the top of the loaded cathode, as shown in Fig. 12, where all boundary conditions are visible in the Abaqus CAE environment. In Fig. 12a, fixed constraints are applied to both ends of the composite assembly to prevent any displacement and rotation around the axis perpendicular to the plane. In Fig. 12b, the loading condition is shown as quasi-static (low-speed impact) and gradual in the perpendicular direction.

In Fig. 12c, due to the position of the rectangular holes (Fig. 11), their displacement by robot number three (shown in Fig. 2a) is allowed along the axis perpendicular to the plane, while other displacements remain fixed. The meshing process was meticulously carried out to ensure accuracy and convergence in the finite element model of the copper-steel-copper composite structure. Adhesive surface elements were employed to model the interfacial contact between the layers, ensuring proper representation of the bonding behavior at the interfaces. The CPE4R elements, a four-node, bilinear, plane strain, reduced-integration quadrilateral element, were selected for its efficiency and suitability for simulating plane strain conditions. This element type was consistently applied across the entire model, including the copper and steel layers, as well as the adhesive interfaces. The mesh size was uniformly set to 1 × 1 mm, ensuring a balance between computational efficiency and solution accuracy. The adhesive surfaces were modeled using a zero-thickness approach.

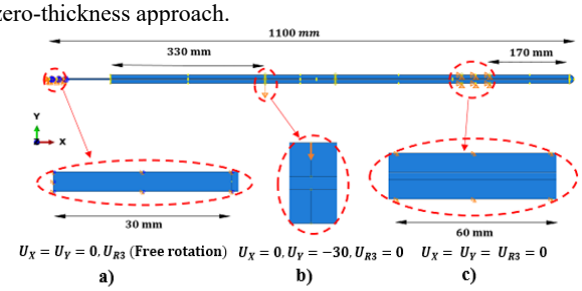


Fig. 12 Boundary conditions and loading setup, including: (a) fixation of the blank, (b) load application position and conditions, and (c) boundary constraints at the cathode composite's end

Fig. 13 illustrates the meshed regions, highlighting the detailed meshing at the interfaces and the overall structure. According to the audit, during the electrorefining process, a certain curvature-induced gap is formed in the shaped cathodes, which has been incorporated into the finite element model as shown in Fig. 13. In summary, the meshing strategy and the use of adhesive surface elements ensured an accurate and efficient representation of the interlayer contact and the overall behavior of the copper-steel-copper composite structure.

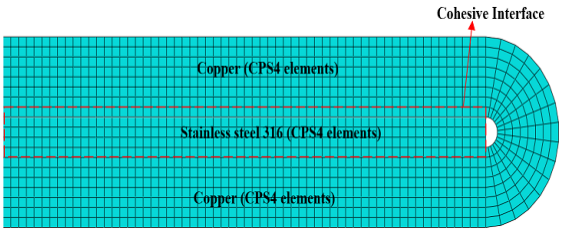


Figure 13. Meshing and adhesive surface elements for interlayer contact and composite components.

8. RESULTS AND DISCUSSIONS

Following the experimental and audit results, the average measured parameters, including the lengths and widths of crack separation and the average thickness of the formed cathode, are reported in Table 4. Point E was defined as the average total length of the crack.

Table 4. Average measured parameters (mm)

F	E	D	C	B	A
7.9	411.33	19.55	29.63	44.33	64.7

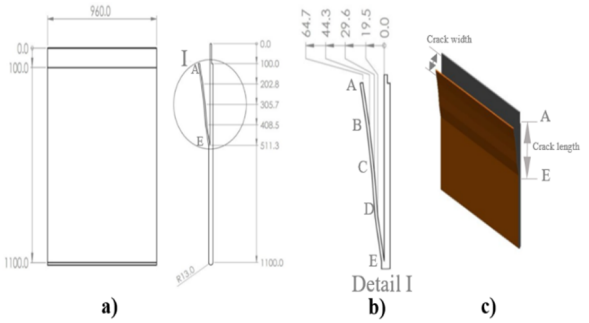


Figure 14. The copper cathode separation from the stainless-steel cathode blank: (a) Front and side view of the transverse crack opening in the cathode and the cathode blank, (b) detailed crack opening measurements along different lengths, (c) three-dimensional representation of the crack formed.

The parameters in Table 4 with geometry locations are shown in Fig. 14. Considering the average of maximum crack opening length (411 mm) and width (64 mm) as a key study parameters with location in cathode separation were addressed in this figure. . In Figure 14(a), the transverse crack opening along the crack opening length is illustrated. The maximum opening width was observed at point (A), and the deformed length of the copper cathode with curvature AE was identified in this section. In Fig. 14b, the transverse opening details at the specified points in Table 4 (A, B, C, D) are presented. The maximum average opening width of the copper cathode, measured at point A, was found to be 64.7 mm, as shown in the detailed illustration (I) in Fig. 14b. This point serves as the reference for evaluating the impact of flex in optimizing numerical comparisons. In Fig. 14c, the experimentally obtained representation based on the average separation of the cathode from the cathode blank, its opening curve according to statistical data, and the average thickness of the formed copper is depicted. The experimental model of the formed cathode after the impact was illustrated. Additionally, the length and width of the crack in the cathode were schematically represented in the measured curvature section.

One of the most critical factors in accurately analyzing industrial problems is the statistical indices related to the operational performance of a device or process [14]. In accordance, the effects of the cathode thickness (denoted by parameter F) on the maximum transverse crack opening width (parameter A) and the maximum crack separation length (parameter E) are analyzed.

8.1. STATISTICAL ANALYSIS

According to the statistical data, the variation trend indicates an inverse relationship between thickness and transverse separation.

From the obtained results, the maximum crack opening occurred in composite No. 2, measuring 87 mm, while the minimum crack opening was in specimen No. 20, measuring 45 mm. Additionally, specimens 1, 2, and 3 exhibited significant crack width, which could be attributed to the lower thickness of the copper layer or the lower fracture energy of the adhesive region formed during the electrorefining process between the cathode and the cathode blank. Specimens No. 9, 20, and 24, which had increased the cathode deposition thickness on the cathode blank, exhibited significantly lower crack openings (below 50 mm). This deviation in crack opening may result from an excessively high copper thickness beyond the normal limit or an increasing fracture energy of adhesive layers. Other contributing factors include ineffective multiple impacts from the flex in separating the cathode from the cathode blank, the formation of an irregular nodule in the impact region, causing slippage, and improper flex contact with the surface. Consequently, a reduction in the contact area during impact also plays a role in this deviation. According to the results in Fig. 15, the average deposited copper thickness is about 7.9 mm, while sheets No. 1 and 3 have lower thicknesses than the average. This discrepancy may be due to non-uniform deposition, errors in the electrorefining process, or chemical inconsistencies in the tank house.

The relationship between cathode thickness and debonding size was quantified using Pearson's correlation coefficient [23]:

$$r = \frac{\sum_{i=1}^{n}(t_i - \bar{t})(d_i - \bar{d})}{\sqrt{\sum_{i=1}^{n}(t_i - \bar{t})^2 \sum_{i=1}^{n}(d_i - \bar{d})^2}} = -0.84 \ (P < 0.001) \quad (8)$$

Where, t_i is the thickness of deposited copper cathode, d_i is debonding size of point A and $n = 24$ is the numbers of cathode. The strong negative correlation ($r = -0.84$ *and* $p = 2.9 \times 10^{-7}$) confirms that as thicker cathodes exhibit smaller debonding or transvers cracks (Fig. 15), and thinner coated copper layers lead to wider cracks width. No. 20 is shown as a maximum crack opening.

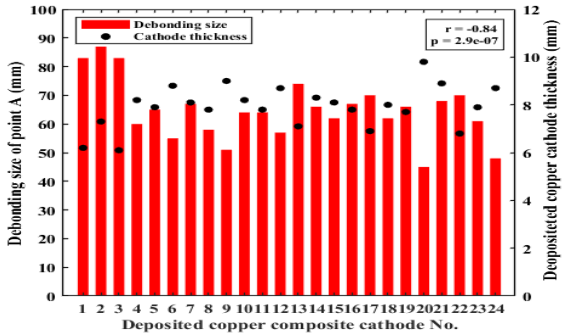


Figure 15. The effects of the thickness of the formed copper layer on the maximum transverse crack opening in a copper-steel-copper composite.

The regression model [24] with the equation of $d = 110.3 - 6.7t$ ($R^2 = 0.67$), in which, slope interpretation shows each 1 mm thickness increase reduces debonding by 6.7 mm. To have a group comparison, cathodes were classified at the median thickness (7.9 mm) into thick (upper median) and thin cathodes (lower median). Thin cathodes ($n = 12$, mean debonding reported as Mean (μ_1) $= 76.3\ mm$ and standard deviation, SD (σ_1) $= 8.2\ mm$. For other samples as thin cathodes, these values are obtained as $\mu_2 = 66.2\ mm$ and $\sigma_2 = 6.9\ mm$, respectively. The differences of $\mu_1 - \mu_2 = 16.1$ shows that the thicker cathode substantially smaller debonding size. The normal distribution of debonding size of width by thickness group is shown in Fig. 16.

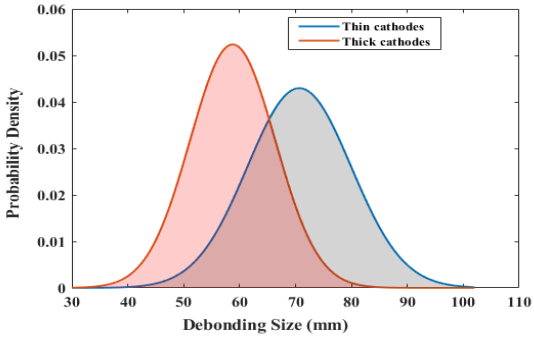


Figure 16. Normal distribution of debonding width size by thickness group

Based on the thickness variations and considering that mechanical parameters such as force and flex position remain constant while the ability to adjust the average thickness variations from a process perspective is currently not feasible, an increase in deposited copper thickness on the cathode blank leads to changes in flex force, increasing interlayer stress during separation and consequently extend the crack opening length. According to the results, in cases where the deposited copper thickness on the cathode blank exceeds the average limit, one potential solution to reduce separation errors is to enhance crack initiation in the adhesive region by modifying the impactor position. Fig. 17 illustrates the effects of the formed copper thickness on the maximum crack opening length. Based on the results, the cathode opening length ranges from 302 to 551 mm, with an average sheet opening length of 411.33 mm at the moment of impact. Sample No. 2 exhibits a significantly larger opening length compared to the average, indicating either a lower copper thickness or reduced fracture energy in the adhesive region. Conversely, Sample No. 20 has a much smaller opening length than the average, which can be attributed to increased fracture energy or excessive deposited copper thickness.

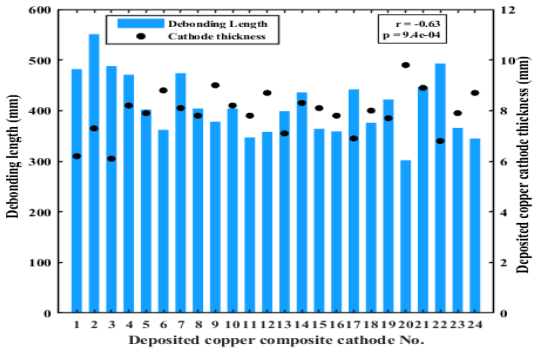


Figure 17. The effects of the thickness of the formed copper layer on the maximum crack opening length in a copper-steel-copper composite.

As a similar analysis of the crack width of point A, Pearson's correlation coefficient and P-value are obtained as ($r = -0.64$ *and* $p = 9.4 \times 10^{-4}$). These parameters show the meaningful inverse relationship between crack length and thickness of deposited copper. The regression model as a linear estimation of dependency data with the equation of $l = 689.2 - 38.5t$ ($R^2 = 0.52$) that slop constant estimated that each 1 mm increase in thickness reduces debonding length by 38.5 mm and 52% of the variability in crack length is explained by thickness changes. The probability density considering two groups of cathode, thin and thick based on average size is shown in Fig. 18. For thin cathode (lower than the average size), Mean $(\mu_1) = 459\ mm$ and SD $(\sigma_1) = 56\ mm$. The curve is centered at 459 mm with moderate spread and 95% fall between 347–571 mm. 68% of thin cathodes fall between 403–515 mm. The thick cathodes are shown by a red curve. In this case, Mean $(\mu_1) = 387\ mm$ and SD $(\sigma_1) = 47\ mm$. A narrower distribution showss more consistent debonding. 68% of thick cathodes fall between 340–434 mm. 95% fall between 293–481. Thin cathodes show wider variability ($\sigma_1 = 56$ versus $\sigma_2 = 47\ mm$, suggesting thicknesses that are lower mean thickness 7.9 mm lead to less predictable debonding. Practically, the thickness below 7.5 mm maximizes the probability of achieving separating upper 500 mm (right tail of the thin-cathode distribution), whereas thicker cathodes provide more consistent but short debonding length.

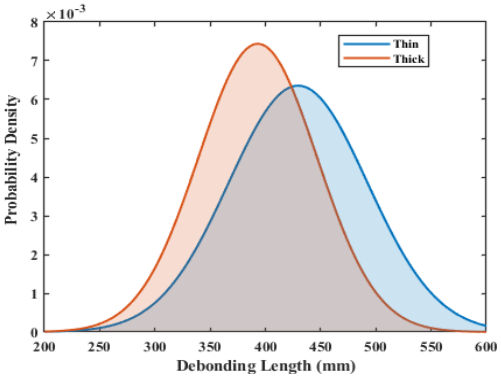


Figure 18. Normal distribution of debonding length size by thickness group

In general, increased opening in the cathode depth within the adhesive region leads to the clearance of space behind the cathode blank, subsequently improving the performance of the second impact during layer deboning. Addressing this issue, which is one of the objectives of this study, will be elaborated in the subsequent sections by proposing a novel design for adjusting the position of the impactor

8.2 FINITE ELEMENT SIMULATION RESULTS

Fig. 19 presents the experimental and validated results obtained under the operational conditions of the stripping section of CSM. Fig. 17a depicts the separation zone and delamination behavior of the cathode in a real situation. Loading was applied in zone 1 as a transverse displacement, with the contact point modeled along a circular arc. Given the device's geometric constraints (with a maximum change in loading capacity dominance 480 mm), loading was analyzed at three distinct zones (1, 2, and 3) located at 330 mm, 405 mm, and 480 mm to evaluate optimal separation performance. The right side of Fig. 19 illustrates a mechanical holder with a contact effect on the cathode, along with fixed constraints implemented in the software to restrict movement. Following the fixation of this region using the holders, an impact was applied to zone 1 of the component by the flex, resulting in the formation of the separation zone, as illustrated in Fig. 19a. Fig. 19b displays the overall stress contour and its correlation with the experimental model. Fig. 19c provides a magnified view of the separation zone (crack). The crack length and width were determined to be 400 mm and 57 mm, respectively. The overall stress contour, predominantly influenced by the stainless-steel core, was also derived in the same figure under the applied loading conditions.

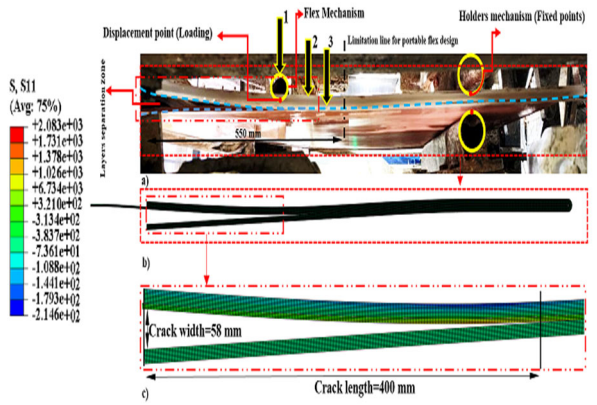


Figure 19. Analysis of separation and cathode etching from the blank: a) experimental setup of the copper cathode delamination plates and loading zones, b) a general view of the separating layers simulation, c) a magnified view of the separation area (crack width and length).

In Fig. 20, the load-displacement of the flex across the three specified regions, with the flex displacement in the CSM device set to 30 mm, is illustrated. The relationship between the applied force and displacement is presented, highlighting the variations in mechanical response due to positional changes. As evident from the results, when the flex shifts from region one to region three, the magnitude of the applied force increases significantly, rising from -602 to -987 KN. This trend indicates that the force exerted on the composite core is highly sensitive to the spatial positioning of the flex.

The observed increase in force suggests that the mechanical interaction between the flex and the composite structure intensifies its movement toward region three. In Fig. 21, the induced stress is depicted for the three respective positions of the flex. The stress profile is evaluated at the point of loading and on the upper copper cathode under bending of composite conditions, specifically within the compressive region.

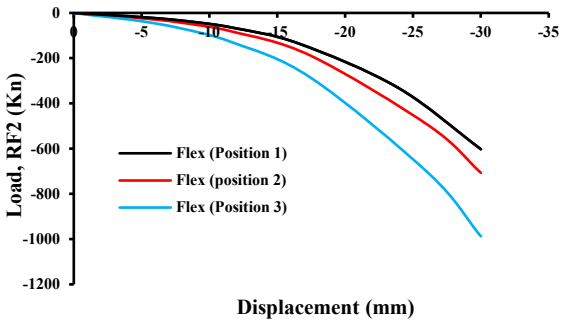


Figure 20. Load-displacement diagram at the point of contact of the flex on the upper copper layer

As illustrated in Fig. 21, when considering the optimal final position in the device, the stress values increase from -731 to -962 MPa. This rise in stress indicates a stronger mechanical response in the system as the flex reaches its optimized position. The results highlight the critical influence of impactor positioning on the stress distribution of the upper copper cathode.

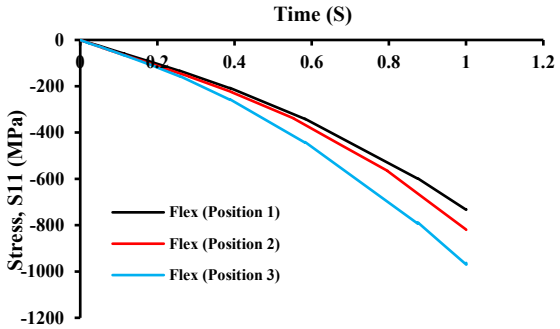


Fig. 21 Stress (S11)-time diagram in the loading region

In Fig. 22, the maximum displacement of the lower edge of the cathode from the cathode blank during loading is illustrated. Fig. 22 demonstrates that shifting the flex position from region 1 to region 2 results in an increase in the displacement of the lower edge of the cathode. Specifically, the displacement rises by 36 millimeters in the optimized condition and by 14 millimeters when considering the impact position in region 2. This variation in displacement highlights the significant positioning of the mechanical behavior of the system.

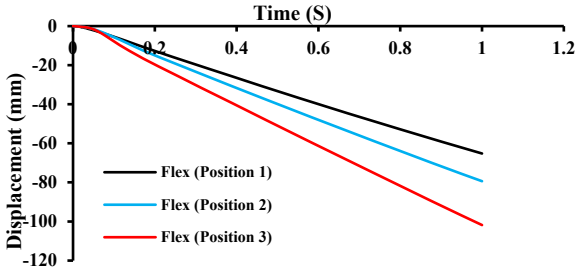


Figure 22. Displacement-time diagram of the maximum cathode edge opening

9. DESIGN OF IMPACT MECHANISM

Table 5 shows the average measured crack parameters for different flex positions. Based on the data in Table 5 and the operational conditions of the device, an impact mechanism was designed, allowing the movement of the flex (as a key component) up to 150 mm above and below the impact line. This design aims to create an asymmetric loading relative to the second flex, which performs the separation of the sheets after the initial flex impact.

Table 5: Average measured crack parameters

Parameters	Position 1	Position 2	Position 3	Difference between variations and the optimal value
Crack width (mm)	58	72	96	38
Crack length (mm)	480	521	578	99

Fig. 23 presents the variations in crack opening parameters under loading conditions, comparing the operational position of the device, the optimal position, and the differences between the reported values. To achieve optimal performance, the mechanism was refined using numerical analyses in Fig. 23, which illustrates the crack opening in both operational and optimal positions. The variation in crack opening from Fig. 23a to 23c in Fig. 10 demonstrates the optimization process of the cathode opening from the cathode blank. In Fig. 21d, a rail was designed to allow the flex to transition from the operational to the optimal position. This rail is designed with the geometry of $400 \times 300 \times 6\, mm^3$. Position 3 is considered as optimal destination design. The new location of the flex mechanism is shown in fig. 23d with the distance of 130 mm from middle of rail.

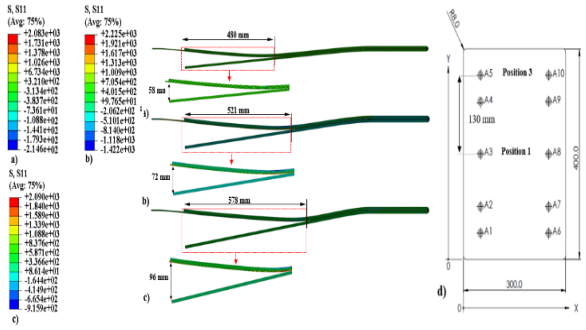


Figure 23. The variations in crack opening parameters under loading conditions for a) flex in position 1, b) flex in position 2, c) flex in position 3, and d) the rail and the optimal installation position of the flex

In Fig. 24, the stages of designing the proposed mechanism and its integration into the CSM device are illustrated. As shown in Fig. 24a, the exploded view of the holder design includes components such as the fixture and other elements. Following the design of this section, a rail is mounted on it, allowing the flex to slide and transfer force optimally as shown in the Fig. 24b. Fig. 24c depicts the overall design of the impact mechanism.

This section is mounted on the impact device (consisting of three sliding parts and a force transmission motor) for an optimal impact, as demonstrated in Fig. 24d.

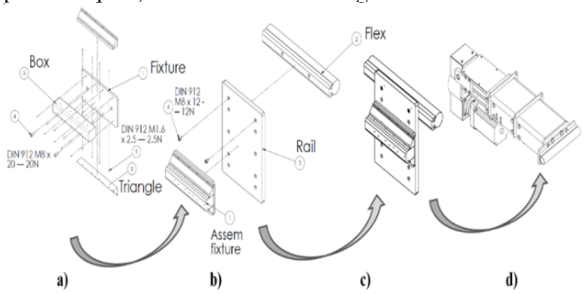


Figure 24. a) Different parts of the new flex mechanism for modern CSM: a) fixture design, b) optimal flex mechanism assembly and related parts, c) mounted mechanism, and d) location of new mechanism installation

10. CONCLUSION

This study aimed to optimize the separation of the cathodes from the cathode blanks in the electrorefining process, addressing critical issues such as inadequate separation and frequent stoppages of the modern CSM machines. Through a comprehensive analysis of the parameters influencing the separation of copper-steel-copper sandwich composite plates, the optimal debonding point was identified using finite element analysis (FEA), cohesive zone model CZM method, and mechanical behavior evaluation under flex impact. Based on the findings, a novel flex impact mechanism was designed and implemented, significantly enhancing the separation efficiency.

The research involved a detailed examination of 24 composite samples, revealing an inverse relationship between the thickness of the deposited copper (ranging from 5 to 10.5 mm) and the delamination parameters (width and length of cracks). For instance, the maximum crack width (87 mm) was observed in specimen No. 2 with the lowest copper thickness, while the minimum crack width (45 mm) was recorded in specimen No. 20 with the highest thickness. Similarly, the maximum crack length (502 mm) was observed in composite No. 2, and the minimum (302 mm) in composite No. 20. These results underscore the critical influence of copper thickness on delamination behavior.

The statistical results show that increasing cathode thickness significantly reduces crack width, with each 1 mm increase decreasing debonding by 6.7 mm. Thick cathodes (upper than 7.9 mm) show 16.1 mm smaller debonding size of point A compared to thin cathodes, confirming thickness as a key factor in controlling interfacial failure. The normal distribution of debonding widths further supports this thickness-dependent behavior. Also, analysis confirms an inverse relationship between copper thickness and crack length ($r = -0.64$, $p < 0.001$), with each 1 mm increase in thickness reducing crack length by 38.5 mm. Thin cathodes (lower than 7.9 mm) exhibit longer but more variable cracks ($\mu = 459$ mm, $\sigma = 56$ mm), while thick cathodes (upper than 7.9 mm) show shorter, more consistent debonding ($\mu = 387$ mm, $\sigma = 47$ mm).

To establish a benchmark for optimization, the average crack length, width, and copper thickness were measured as 411 mm, 64 mm, and 7.9 mm, respectively. Given the constraints in accessing chemical process parameters such as nodule formation, fracture energy, and adhesive zone properties, the study focused on mechanical optimization. Three loading positions (330 mm, 405 mm, and 450 mm) were analyzed to determine the optimal flex impact location. The results demonstrated that positioning the flex at 480 mm from the top of the cathode yielded the most effective mechanical performance, increasing crack width from 58 mm to 96 mm, crack length from 480 mm to 578 mm, and generated stresses (S_{11}) from -731 to -962 MPa and a maximum copper edge displacement of 36 mm.

Based on mechanical separation composite layers improvement, an optimized flex mechanism, a fixture, rail, and auxiliary components were designed and integrated into the CSM machine. This mechanism, capable of asymmetric impact and extended delamination, ensures efficient cathode-cathode blank separation in copper electrorefining processes. The improvements not only enhance the operational efficiency of the CSM machine but also reduce unplanned downtime, offering significant economic and operational benefits.

This research provides valuable insights into the mechanical m echanisms of delamination and offers a practical solution for o ptimizing stripping in modern CSMs. The findings lay the gro undwork for future studies exploring advanced composite mat erials and environmental factors to further refine flex mechani sms and separation efficiency.

AUTHOR'S CONTRIBUTION

Mohsen Forouzanmehr performed data analysis, numerical simulation, and wrote the manuscript. Mohammad Reza Dashtbayazi supervised the project and revised the manuscript. Masoud Raoufi Jahromi collected data and wrote the manuscript. Seyedhamed Pourbagheri facilitated the use of equipment and devices at the copper refinery of Sarcheshmeh. All authors discussed the results and contributed to the final manuscript.

This project is done as a part of the SBUK audit team.

REFERENCES

[1] M. E. Schlesinger, K. C. Sole, and W. G. Davenport, Extractive metallurgy of copper .Elsevier, 2011, https://doi.org/10.1016/C2010-0-64841-3

[2] N. Aslin, O. Eriksson, G. Heferen, and G. S. Yek, "Developments in Cathode Stripping Machines - An Integrated Approach for Improved Efficiency," Proceedings of Cu, p. 1, 2010.

[3] M. Shojaei, G. R. Khayati, S. M. J. Khorasani, and R. K. Hernashki, "Investigation of spring back phenomenon in the 316L stainless steel cathode blank based on the changes in electrical resistivity and magnetic properties due to the residual stress and martensite phase formation: an industrial failure," Engineering Failure Analysis, vol. 126, p. 105473, 2021, https://doi.org/10.1016/j.engfailanal.2021.105473

[4] K. Wu et al., "Interfacial strength-controlled energy dissipation mechanism and optimization in impact-resistant nacreous structure," Materials & Design, vol. 163, p. 107532, 2019, https://doi.org/10.1016/j.matdes.2018.107532
[5] W. Armstrong and C. Refineries, "The ISA PROCESS and its contribution to electrolytic copper," Rautomead Conference, Scotland, 1999.
[6] F. Volpi et al., "A capacitance-based solution to monitor absolute crack length in four-point bending test: Modelling and experiments," Sensors and Actuators A: Physical, vol. 254, pp. 145-151, 2017, https://doi.org/10.1016/j.sna.2016.12.017
[7] D. Höwer, B. A. Lerch, B. A. Bednarcyk, E. J. Pineda, S. Reese, and J.-W. Simon, "Cohesive zone modeling for mode I facesheet to core delamination of sandwich panels accounting for fiber bridging," Composite Structures, vol. 183, pp. 568-581, 2018, https://doi.org/10.1016/j.compstruct.2017.07.005
[8] X. Zhang, Z.-y. Cai, J.-x. Gao, and M.-w. Wang, "Numerical analysis of face sheet/core debonding failure in the plastic forming of aluminum foam sandwich panel," The International Journal of Advanced Manufacturing Technology, vol.128,no.5-6,pp.2285-2300,2023, https://doi.org/10.1007/s00170-023-12087-5
[9] J. Correia, R. Campilho, R. Rocha, Y. Liu, and L. Ramalho, "Parametric study of composite curved adhesive joints," The International Journal of Advanced Manufacturing Technology, vol. 111, pp. 2957-2970, 2020, https://doi.org/10.1007/s00170-020-06314-6
[10] B. Aryal, E. Morozov, H. Wang, K. Shankar, P. Hazell, and J. Escobedo-Diaz, "Effects of impact energy, velocity, and impactor mass on the damage induced in composite laminates and sandwich panels," Composite Structures, vol. 226, p. 111284, 2019, https://doi.org/10.1016/j.compstruct.2019.111284
[11] N. Almeida, V. Ciminelli, P. Cetlin, and D. Majuste, "Cathode stripping behavior: Simulation by the finite element method and experimental effect of cathode surface roughness and its repeated use," Hydrometallurgy, vol. 220, p. 106103, 2023, https://doi.org/10.1016/j.hydromet.2023.106103
[12] W. Chen, F.-l. Huang, Z.-h. Zeng, Z.-j. Wang, and A.-g. Pi, "Microstructure and mechanical properties of heterogeneous-gradient composite plates with a sphere-array interlayer prepared using explosive welding," Journal of Materials Research and Technology, vol. 30, pp. 6508-6519, 2024, https://doi.org/10.1016/j.jmrt.2024.05.054
[13] M. Boomeri, K. Nakashima, and D. R. Lentz, "The Sarcheshmeh porphyry copper deposit, Kerman, Iran: A mineralogical analysis of the igneous rocks and alteration zones including halogen element systematics related to Cu mineralization processes," Ore Geology Reviews, vol. 38, no. 4,pp.367-381,2010, https://doi.org/10.1016/j.oregeorev.2010.09.001
[14] S. Shakibania, M. Mokmeli, and S. M. J. Khorasani, "Statistical analysis of factors affecting the anode scrap rate at the Khatoon Abad Copper Refinery Plant," Metallurgical and Materials Transactions B, pp. 1-16, 2022, https://doi.org/10.1007/s11663-021-02373-6
[15] A. Morales-Aragon, D. Sánchez-Rodas, G. Ríos, and M. S. Moats, "Impurity Behavior in Cast Copper Anodes: Implications for Electrorefining in a Circular Economy," Metals,vol.15,no.2,p.113A,2025, https://doi.org/10.3390/met15020113
[16] M. Chen, X. Xiao, H. Guo, and J. Tong, "Deformation behavior, microstructure and mechanical properties of pure copper subjected to tube hydroforming," Materials Science and Engineering: A,vol.731,pp.331-343,2018, https://doi.org/10.1016/j.msea.2018.06.068
[17] J. Horak, V. Sikka, and D. Raske, "Review of mechanical properties and microstructures of Types 304 and 316 stainless steel after long-term aging," Oak Ridge National Lab., TN (USA); Argonne National Lab.,IL(USA),1983, https://www.osti.gov/biblio/588934
[18] K. Park and G. H. Paulino, "Cohesive zone models: a critical review of traction-separation relationships across fracture surfaces," Applied Mechanics Reviews, vol. 64, no. 6, p. 060802, 2011, https://doi.org/10.1115/1.4023110
[19] C. Sarrado, F. A. Leone, and A. Turon, "Finite-thickness cohesive elements for modeling thick adhesives," Engineering Fracture Mechanics, vol. 168, pp.105-113,2016, https://doi.org/10.1016/j.engfracmech.2016.03.020
[20] P. Papanastasiou and E. Sarris, "Cohesive zone models," in Porous rock fracture mechanics: Elsevier, 2017, pp. 119-144, https://doi.org/10.1016/B978-0-08-100781-5.00006-3
[21] P. Saikia and N. Muthu, "Estimation of CZM Parameters for Investigating the Interface Fracture of Adhesively Bonded Joints Under Mode I, Mode II, and Mixed-Mode (I/II) Loading," Fatigue & Fracture of Engineering Materials & Structures, vol. 47, no. 12, pp.4636-4649,2024. https://doi.org/10.1111/ffe.14457
[22] A. Akhavan-Safar, E. A. Marques, R. J. Carbas, and L. F. da Silva, "Cohesive Zone Modelling - CZM," in Cohesive Zone Modelling for Fatigue Life Analysis of Adhesive Joints: Springer, 2022, pp. 19-42, https://doi.org/10.1007/978-3-030-93142-1
[23] P. Sedgwick, "Pearson's correlation coefficient," Bmj ,vol. 345, 2012, https://doi.org/10.1136/bmj.e4483
[24] K. B. Keerthana, S.-W. Wu, M.-E. Wu, and T. Kokulnathan, "The United States energy consumption and carbon dioxide emissions: a comprehensive forecast using a regression model," Sustainability, vol. 15, no. 10, p. 7932, 2023. https://doi.org/10.1136/bmj.e4483